Ultrasonics Sonochemistry 125 (2026) 107741

Contents lists available at ScienceDirect

Ultrasonics Sonochemistry

journal homepage: www.elsevier.com/locate/ultson

The importance of (un)dissolved gases on early-stage cavitation dynamics within an acoustic field

Erçil Toyran, Mojca Zupanc, Martin Petkovsek, Matevz Dular *

Faculty of Mechanical Engineering, University of Ljubljana, Askerceva 6, 1000 Ljubljana, SI, Slovenia

ARTICLE INFO

Keywords:
Cavitation
Gas content
Ultrasonic horn
Bubble

ABSTRACT

Gas content strongly affects cavitation dynamics; however, most studies rely solely on dissolved gas measurements, overlooking the influence of undissolved bubbles. This study investigates their role by introducing air bubbles (<200 μm) into water samples with identical dissolved gas levels and analyzing cavitation at both inception and developed phases using high-speed imaging and hydrophone measurements. The results show that the presence of pre-existing bubbles alters cavitation dynamics at the inception and developed phases. Under low dissolved gas and in the absence of air bubbles, cavitation can initiate from a single nucleus, and the developed phase exhibits transient vaporous cavitation with the highest acoustic intensity. In contrast, pre-existing bubbles promote the formation of conical-like bubble structures early in the inception phase and affect their dynamics in the developed phase, reducing the acoustic pressure and attenuating the noise spectrum. These effects are reversible upon bubble removal and independent of dissolved gas concentration, demonstrating that dissolved gas alone cannot represent gas-related influences on cavitation. Characterizing not only dissolved but also undissolved gas content is therefore essential for cavitation studies and applications.

1. Introduction

Cavitation occurs when the static pressure within the fluid/liquid drops below the vapor pressure at a specific temperature which results in gas/vapour bubble formation [1]. Upon pressure recovery the bubbles collapse leading intense effects, such as shockwaves, microjets, local temperature increase (according to the hot spot theory: about 5000 K [2]) which can trigger highly reactive radical formation (like hydroxyl radicals $^{\bullet}$OH) [1,3]. Cavitation was traditionally mitigated to prevent malfunction and erosion in turbomachinery, but nowadays the research is focused to its energy harnessing and using it in various engineering applications. Its potential extends even to current and future global challenges, such as biomedical applications, wastewater treatment, emulsification, and biomass processing [4–9].

Accordingly, understanding and characterizing cavitation are key to its control and further standardize and effectively scale cavitation processes. To this end, there are some simple approaches that have been used. For example, in hydrodynamic cavitation research cavitation number is often used to characterize flow conditions. It is a dimensionless number that defines how close the system pressure to vapor pressure is, relative to the dynamic pressure at specific temperature and has been used to describe cavitation inception, intensity and chemical effects [10–12]. Moreover, a similar parameter has been proposed for acoustic cavitation [13]. Nevertheless, the reliability of cavitation number is debated [14–16]. One of the key limitations, even when one considers all the geometric specifics of the system, is that it does not capture the quality of the liquid. As demonstrated by Keller, cavitation is extremely sensitive to the water quality and even a small change in water quality may result in large differences in cavitation inception number leading to inconsistencies in experimental observations even under identical geometrical and flow conditions [17]. Such deviations can be attributed to variations in tensile strength and further on the concentration and size of nuclei within the liquid, which are related to its gas content [17,18]. These nuclei, often described as tiny gas bubbles, decrease the cavitation threshold facilitating liquid–gas transition according to the concept of heterogeneous nucleation. They may exist freely in the bulk liquid or be trapped in the crevices of solid particles or surfaces [12,19].

The gas content of a liquid is given by the sum of dissolved and undissolved gases (free or attached bubbles). Its effect on cavitation has been widely investigated, and it extends beyond inception, where gas bubbles can act as cavitation nuclei, while the gases dissolved in the bulk

* Corresponding author.
E-mail address: matevz.dular@fs.uni-lj.si (M. Dular).

https://doi.org/10.1016/j.ultsonch.2026.107741
Received 19 November 2025; Received in revised form 24 December 2025; Accepted 7 January 2026
Available online 8 January 2026

liquid help stabilize these nuclei through gas diffusion [12]. Although some hypotheses suggest that dissolved gases may act as weak points in the liquid together with pre-existing bubbles, this has not yet been clearly demonstrated experimentally[20]. For example, Li et al. [21] investigated the effect of dissolved oxygen and nitrogen on cavitation inception and reported that dissolved oxygen reduces the tensile strength of water stronger than nitrogen, possibly due to greater depletion of water molecules around oxygen. Still, dissolved gases are important because cavitation bubbles contain a certain amount of gas, the amount of which is influenced by the dissolved gas concentration in the surrounding liquid. Analytical studies have shown that variation in the bubble gas content alters bubble collapse dynamics, thereby influencing both the intensity and the nature of the collapse event [22,23].

It is many times neglected (possibly due to nontrivial measurements) that the role of undissolved bubbles bears an even greater importance for cavitation. The influence of free gas bubbles on cavitation extends beyond their role as cavitation nuclei. Single-bubble cavitation studies have shown that neighboring gas bubbles can strongly influence cavitation bubble dynamics, including collapse intensity, collapse direction, and oscillation time, highlighting that the number, radius, and distance of the gas bubbles are important parameters [24–27]. In these studies, gas bubbles were generated in a controllable way with respect to their diameter and number. In studies on hydrodynamic and acoustic cavitation, gas bubbles can be injected into bulk liquid to control cavitation, with the process regulated by experimental parameters such as gas flow rate or the nozzle size of the diffuser. Drag reduction by injecting air bubbles in hydrodynamic cavitation can be given as an example [28]. However, gas bubbles also pre-exist in the bulk liquid influencing cavitation. For example, presence of free nuclei can alter the development and inception of sheet cavitation or in acoustic cavitation could modify the topology and the dynamics of cavitation structures [29,30]. Moreover, under acoustic field gas bubbles change the compressibility of the liquid and could attenuate the acoustic field through absorption and scattering [1,31,32].

As mentioned, in experimental studies, the undissolved gas presence is many times neglected or at best characterized indirectly through dissolved gas measurements – mainly due to the fact that quantification and control is challenging. The most common gas content measurement technique is the use of dissolved oxygen sensors, since they are widely available on the market and easy to use [21,33–35]. The basic reasoning is that a higher dissolved oxygen level corresponds to a higher total dissolved gas level, and thereby a higher free gas bubble/nuclei content, and vice versa. For example, Liu et al. [35] used this approach and showed that cavitation intensity, measured by a hydrophone in an ultrasonic bath, initially increases as gas bubble density decreases with lower dissolved oxygen levels, but decreases again once the dissolved oxygen level falls below a certain threshold because too few nuclei remain in the liquid. Similar correlations between dissolved oxygen concentration and gas bubble content have also been reported in other studies [36–38]. However, neglecting the preexisting gas bubbles/nuclei or their indirect characterization by dissolved oxygen sensors can be misleading especially for liquids which can include bubbles like tap water. Since undissolved gas bubbles play a prominent role in cavitation, their proper characterization prior to cavitation experiments is crucial.

In the present study, we aim to demonstrate that the measurements of dissolved oxygen quantity alone are not sufficient to fully characterize the gas-related influences on cavitation. For this, the effect of pre-existing air bubbles on ultrasonic cavitation performance in deionized water samples with similar dissolved oxygen content was investigated using high-speed imaging and hydrophone measurements. The undissolved bubble content was systematically introduced using an air sparging method prior to the cavitation experiments. After sparging, the microbubbles (< 200 μm) remaining in the liquid were characterized with respect to their size and density through visualization. The present approach separates the effects of dissolved oxygen and undissolved gas content, highlighting the limitations of using dissolved oxygen measurements as the sole indicator of gas content in cavitation studies.

2. Methods

2.1. Experimental setup

The experimental setup shown in Fig. 1 consists of a piezoelectric transducer with a driving frequency of 20 kHz (UIP1000hdT, Hielscher Ultrasonics), a high-speed visualization system, and a hydrophone measurement system.

The ultrasonic transducer was equipped with a cylinder-shaped horn with a tip diameter of 15 mm. In all the experiments, the transducer was immersed in the liquid to a depth of 15 mm to maintain consistent energy delivery and set to 40 % of its maximum amplitude. For the high-speed visualization, a Photron Fastcam SA-Z high-speed CMOS camera was employed at a frame rate of 200,000 fps with a resolution of 280 x 640 pixels and exposure time of 2.5 μs to capture the fast transient cavitation dynamics. The high-speed camera was equipped with 105 mm Nikkor lens with backlight illumination provided by high power LEDs. Acoustic noise was measured using a hydrophone (TC4013, Teledyne Marine) immersed to a depth of 35 mm at a fixed position approximately 10 mm away from the sonotrode. Measurements were performed after the onset of cavitation, ensured by waiting 3 s after activation of the ultrasonic transducer, and acoustic emissions were recorded over the subsequent 3 s interval. A short time window was selected to minimize the influence of cumulative thermal effects, time-dependent gas dissolution processes, and the overall degassing effect of acoustic cavitation. The hydrophone is omnidirectional and has a calibrated frequency response in the range of 1 Hz to 170 kHz. The hydrophone signal was amplified by 10 dB and filtered by a charge amplifier (Reson VP2000). This signal was transferred to the workstation through a data acquisition device (NI 9222 – National Instruments). The raw data was stored in the workstation for further signal analysis by MATLAB. The signal analysis included Sound Pressure Level (SPL) calculations using Fourier based methods, as well as Root Mean Square (RMS) analysis. The obtained time domain signals were converted to acoustic pressure using calibration factor considering the hydrophone sensitivity and the + 10 dB gain of the charge amplifier. Then the SPL spectrum was obtained using Welch's method [39] in MATLAB. Using the mentioned methods, the cavitation events in liquid samples with varying gas content were evaluated. The overall pressure signal amplitude was quantified using RMS analysis.

2.2. Sample preparation

The sample preparation and the subsequent experiments were carried out at room temperature (24 ± 1 °C). Liquid samples with low dissolved gas levels were prepared by degassing with a vacuum pump, and simultaneous stirring by a magnetic stirrer. This resulted in

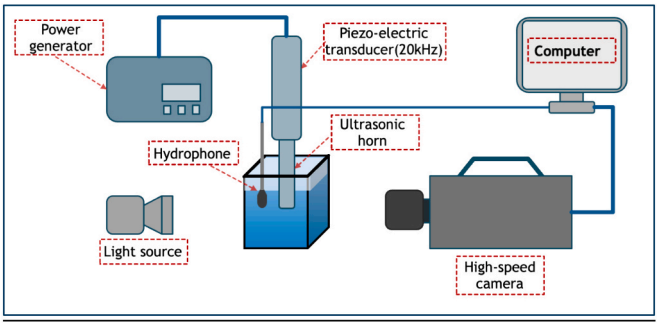

Fig. 1. Experimental setup used in acoustic cavitation experiments including hydrophone measurement and high-speed imaging systems.

accelerated gas removal and further elimination of undissolved bubbles, which may be present in an untreated sample. To prepare water samples with similar dissolved oxygen content and varying undissolved bubble content, first the liquid was left under ambient conditions to reach air saturation overnight. Thereafter, air sparging was performed in the setup shown in Fig. 2a. In this setup, compressed air was introduced into the sample cylinder, which was filled with 250 ml of deionized water. The compressed air was introduced into the liquid from the bottom upwards, with the air pressure controlled by a pressure regulator and a pressure transducer. Sparging was performed at 2 bar absolute pressure for 1 min. The sample cylinder remained open to the atmosphere to prevent pressure build-up. Under these conditions, the dissolved oxygen level did not change significantly (≈0.3 mg/L), while the undissolved bubble content was modified. Prior to cavitation experiments the air sparged liquid was left to rest for 1 min to allow larger bubbles to rise and escape. To further modify the undissolved gas content these samples were mixed in a closed beaker using a magnetic stirrer at 500 rpm for 10 mins, leading to rise and escape of bubbles.

Before and after all the treatments, dissolved gas level and temperature of the liquid were measured. Dissolved gas measurements were carried out using a dissolved oxygen sensor (VisiFerm mA 325 with H4 cap, Hamilton). To prevent gas exchange between air and sample, the measurements were carried out in a closed system (Fig. 2b).

To visualize and quantify undissolved air bubbles, a thin 20 mm × 20 mm microscope slide was gently placed on the liquid surface of 40 mm x 40 mm x 110 mm glass container, 1 min after sparging was completed (Fig. 2c). Once placed, the slide remained stable at the center of the liquid surface due to surface tension, which supported its weight and prevented movement during the bubble collection. After an additional 2 min, air bubbles collected beneath the slide. The waiting time (1 + 2 min) was chosen to achieve maximum yield while minimizing bubble coalescence. The trapped bubbles were then imaged by a camera (LEO2 5000S-24GM, Vision datum) with a resolution of 2448x2048 pixels, and their size distribution and number density were analyzed using ImageJ. During the image processing, diameters below 20 μm were excluded to avoid sub-resolution noise. Sample images of undissolved air bubbles are shown in Fig. 3.

As one can see in Fig. 3, the saturated liquid contains no undissolved gases (a). The highest undissolved air bubble content is obtained in air sparged liquid, when the liquid is left to rest (b). When the liquid is mixed after the sparging the undissolved gas content is gradually reduced to only few undissolved bubbles after 10 mins of mixing (c). For the vacuumed samples (conditions 1 in Table 1) there were of course no undissolved air bubbles present in the samples.

Four different water samples were prepared. Table 1 gives their dissolved oxygen (DO) content and undissolved air bubble characteristics.

3. Results & discussion

3.1. Cavitation inception

Gas content effect on cavitation inception was investigated via high-speed imaging. Gas content was evaluated for both the dissolved and undissolved gases in the liquid. For this, 3 different conditions were investigated including samples with low dissolved gas (condition 1) and two additional air-saturated samples containing the same amount of dissolved oxygen but differing in terms of undissolved gas content: one with no (condition 2) and one with high observed bubble content (condition 3).

Cavitation inception at these conditions is shown in Fig. 4. In condition 1, due to the low DO content, cavitation inception can occur from a single nucleus (Fig. 4b). The bubble expands during the compression phases and subsequently collapses (Fig. 4c). This collapse generates multiple nuclei, leading to the development of a grape-like bubble cluster consisting of multiple small bubbles (Fig. 4d).

When the gas content of the liquid is at the saturation level with no observed pre-existing bubbles (condition 2), cavitation initiates from multiple positions on the surface of the sonotrode, as shown in Fig. 4e. The bubbles merge into small clusters, which oscillate in phase with the driving frequency of the sonotrode (Fig. 4f). As the process continues, cavitation develops downwards, forming streamer like structures beneath the tip (Fig. 4g). The firstly separated cavitation clouds gradually coalesce toward the central region below the sonotrode, eventually forming a large, stable cavitation cloud in the center of the tip (Fig. 4h). The migration towards the center may be attributed to the initially unstable acoustic field affecting the pressure gradient, since the sonotrode was activated only shortly before.

Compared to condition 1 (Fig. 4a – d), characterized by a low dissolved gas level, multiple cavitation inception points appear in condition 2 (Fig. 4e – h), suggesting a higher number of cavitation nuclei. Although undissolved bubbles are not detected in either case, it is reasonable to assume that air saturated sample may contain microbubbles below the detection limit of the bubble screening method working as nucleation points.

By keeping the dissolved gas level constant as in condition 2 and increasing the pre-existing bubble content (condition 3), several phenomena can be observed near the sonotrode tip. In condition 3, pre-existing bigger bubbles tend to move away from the tip while the smaller bubbles stay and oscillate after sonotrode activation (Fig. 4j). During oscillation, the surface-attached bubbles undergo fragmentation, producing smaller bubbles, which accumulate near the center (Fig. 4k). Simultaneously, pre-existing air bubbles in the bulk liquid are attracted toward the center of the tip, where they contribute to the increase in local bubble concentration (see also Video 1 in the Supplementary material). This behavior can be attributed to the primary Bjerknes forces

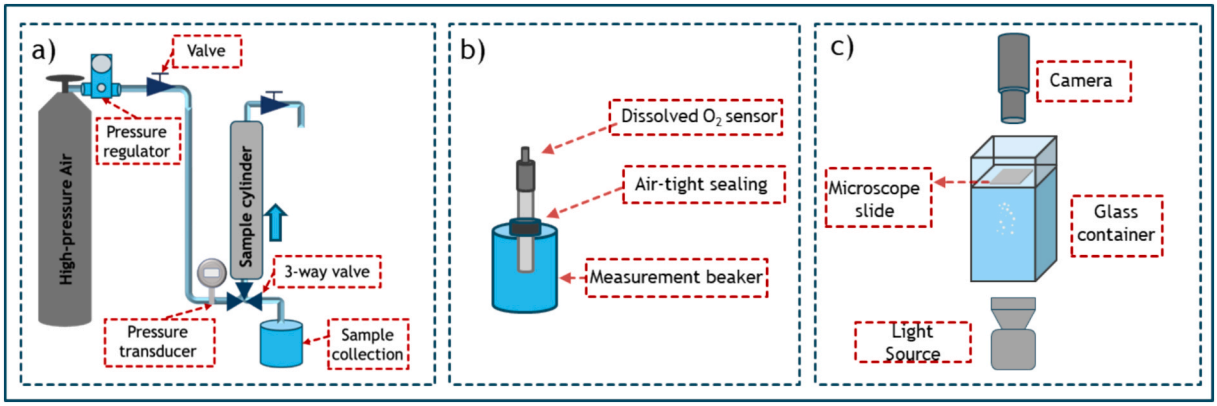

Fig. 2. Representation of the methods used for (a) air sparging, (b) dissolved oxygen measurement, and (c)air bubble visualization.

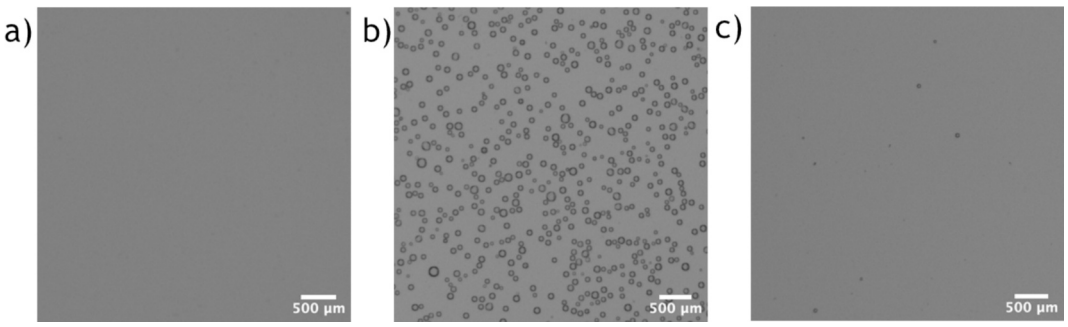

Fig. 3. Visualization of undissolved bubbles: (a) air-saturated liquid (condition 2 in Tab 1), (b) air sparged liquid (condition 3), (c) 10 min mixing after air sparging (condition 4).

Table 1
Properties of prepared liquid samples. Note: N/A indicates not applicable.

Condition	DO (mg/L)	Mean bubble diameter (μm)	SD between replicates (μm)	Mean bubble density (bubbles/mm^2)	Bubble Density SD
1. Vacuumed	4.2	N/A	N/A	N/A	N/A
2. Saturated	8.4 ± 0.18	N/A	N/A	N/A	N/A
3. After air sparging	8.7 ± 0.12	87.4	± 8.1	19.5	± 2.2
4. After air sparging + 10 mins mixing	8.6 ± 0.14	68.3	± 2.7	0.25	± 0.08

[40], as the pre-existing bubbles, with diameters below 200 μm, are sub-resonant and thus experience a net attraction toward the pressure antinode located at the sonotrode tip. This behavior can also be attributed to bubble–bubble interactions, where the secondary Bjerknes force attracts nearby free bubbles toward oscillating ones near the sonotrode tip, as previously reported by Yasui [41]. Consequently, the agglomeration of the bubbles forms a thin bubbly film, which periodically appears and collapses in synchrony with the driving frequency. The film eventually thickens and begins to eject bubbles downwards (Fig. 4l, see also Video 1 in the Supplementary material), where they organize into a conical bubble structure (CBS) beneath the sonotrode (Fig. 4m). Similar formation was observed by Bai et al. [42] who introduced artificial nuclei near the sonotrode tip through a needle. They reported that when these bubbles impacted the radiating surface, they temporarily covered the sonotrode face and reorganized into a CBS, termed the "artificial" CBS. They also observed a similar phenomenon when placing a metal net in front of the sonotrode supplying bubble nuclei on it [43]. As the nuclei are pre-existing in the bulk liquid, the structure observed here corresponds to a naturally promoted CBS formation rather than an artificially induced one. In this case, the pre-existing bubbles primarily contribute to the formation of the surface-attached bubbly film that precedes the development of the CBS, consistent with the mechanism described by Dubus et al. [44]. Accordingly, these observations indicate that the presence of pre-existing gas nuclei in the bulk liquid, even under similar dissolved gas conditions as in condition 2, promotes the establishment of the CBS during the early stages of cavitation.

To further investigate cavitaiton inception from a single free bubble beneath the vibrating sonotrode, we return to condition 1, which

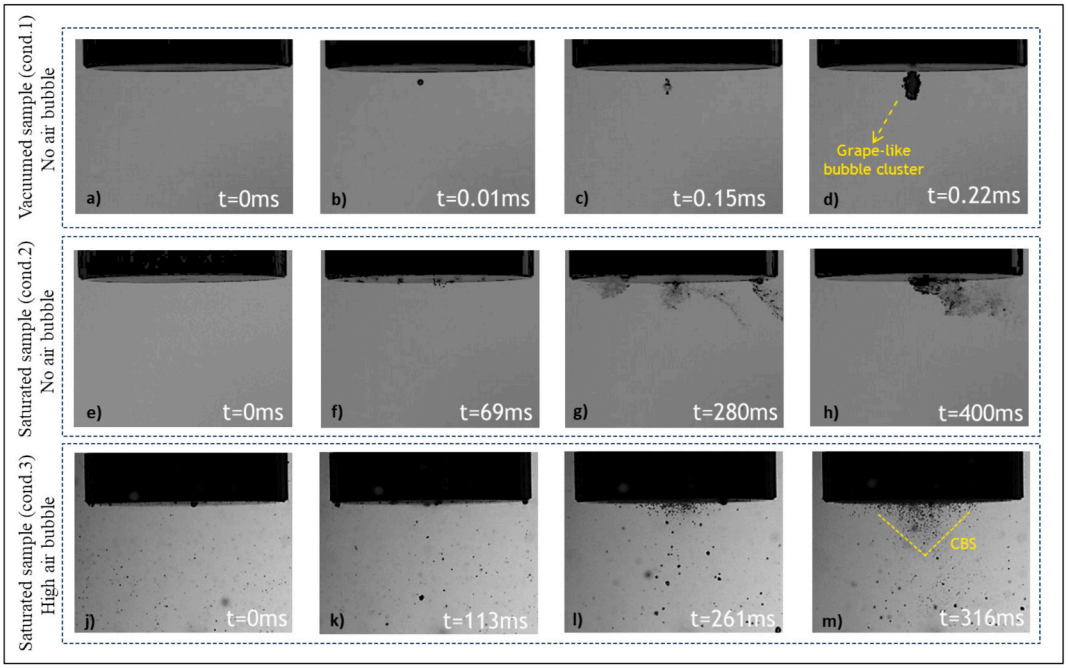

Fig. 4. Incipient cavitation in three water samples: (a–d) vacuumed sample with low dissolved oxygen (condition 1), (e–h) gas-saturated sample without pre-existing bubbles (condition 2), and (j–m) gas-saturated sample containing pre-existing air bubbles (condition 3).

uniquely shows this behavior. Fig. 5 displays 27 successive frames capturing its growth–collapse cycle.

Before cavitation inception there were no visible preexisting air bubbles beneath the sonotrode tip or in the bulk liquid. The first bubble can be observed at t = 0.01 ms located near to the center of the sonotrode. As the acoustic pressure drops during the rarefaction phase, the bubble undergoes volumetric expansion and reaches its maximum radius at t = 0.02 ms. With the reduction in acoustic pressure, the initial spherical bubble shrinks, and jet formation occurs away from the transducer, and become visible at t = 0.05 ms. Following the jet formation, the bubble does not collapse completely, likely due to the lower surrounding pressure during the rarefaction phase. In the following frames (t = 0.06–0.08 ms), the cavitation bubble rebounds, the asymmetry gradually decreases, and the bubble becomes nearly spherical again at t = 0.09 ms. In the next frame (at t = 0.10 ms), one can see that the bubble loses its spherical symmetry and develops a sharp inward curvature directed toward the sonotrode marking the initiation of the collapse phase. This observation suggests the onset of a jet which is clearly observed in the following frames (t = 0.11–0.14 ms). In the next frame (t = 0.15 ms), the bubble collapses, leaving behind a number of "daughter" bubbles, which serve as precursors to cloud cavitation development by providing nuclei. Thereafter, the bubble cloud grows and oscillates along the center of the transducer and finally collapses after 0.09 ms (at t = 0.26 ms), within a period, which corresponds roughly to the findings of Žnidarčič et al. [37,45].

3.2. Visualization and noise frequency spectra

Moving from the cavitation inception, the effect of gas content on developed cavitation was investigated using hydrophone noise measurements in conjunction with high-speed imaging. The same conditions as in section 3.1 were used, including condition 1, which has the lowest DO content; condition 2, which is air-saturated; and condition 3, which has the same DO level as condition 2 but a higher undissolved gas content.

The results (Figs. 6–8) show the power spectral densities (PSD) of the grayscale intensity of the visualizations, coupled with the SPL of the acoustic noise up to 50 kHz, corresponding to the Nyquist limit of the visualization system. This method allows us to compare the cavitation density and the intensity of cavitation noise at specific frequencies.

When the DO level is reduced to 4.2 mg/L (condition 1), which is approximately half of the ambient air-saturation level, the developed cavitation beneath the sonotrode appears as shown in Fig. 6c. The cavitation structure oscillates at the driving frequency of 20 kHz, consistent with the dominant peak (at 20 kHz) observed in both the PSD of grayscale intensity (Fig. 6a) and the SPL of acoustic noise (Fig. 6b). During each oscillation cycle, the cavitation cloud collapses, leaving "daughter" bubbles that persist for a short time between successive frames, as seen in the high-speed visualizations (Fig. 6c at t = 0.05 ms). The remaining bubbles act as precursors for cavitation in the next acoustic cycle. In addition to the attached cloud, the cavitation appears dispersed and irregular, consisting of small individual bubbles and short bubble streams in the background. The origin of these are likely sub-resolution microbubbles. Bursting cavitation activity is observed in the "background" as a low-frequency component around $f_0/8 \approx 2.5$ kHz. This bursting cavitation behavior can be primarily associated with transient cavitation cloud activity rather than stable single-bubble oscillations, and the appearance of subharmonic components such as $f_0/8$ may therefore be related to collective cloud dynamics [46–48]. In this context, the concurrent presence of higher-order subharmonics and a broadband noise increase can be considered consistent with the subharmonic route to chaos described by Lauterborn and Cramer [46]; however, further investigation beyond the scope of the present study would be required to fully verify and characterize this behavior. This behavior can be seen in Fig. 6a in the gray scale intensity and in the corresponding noise data (Fig. 6b) as small peaks. However, the

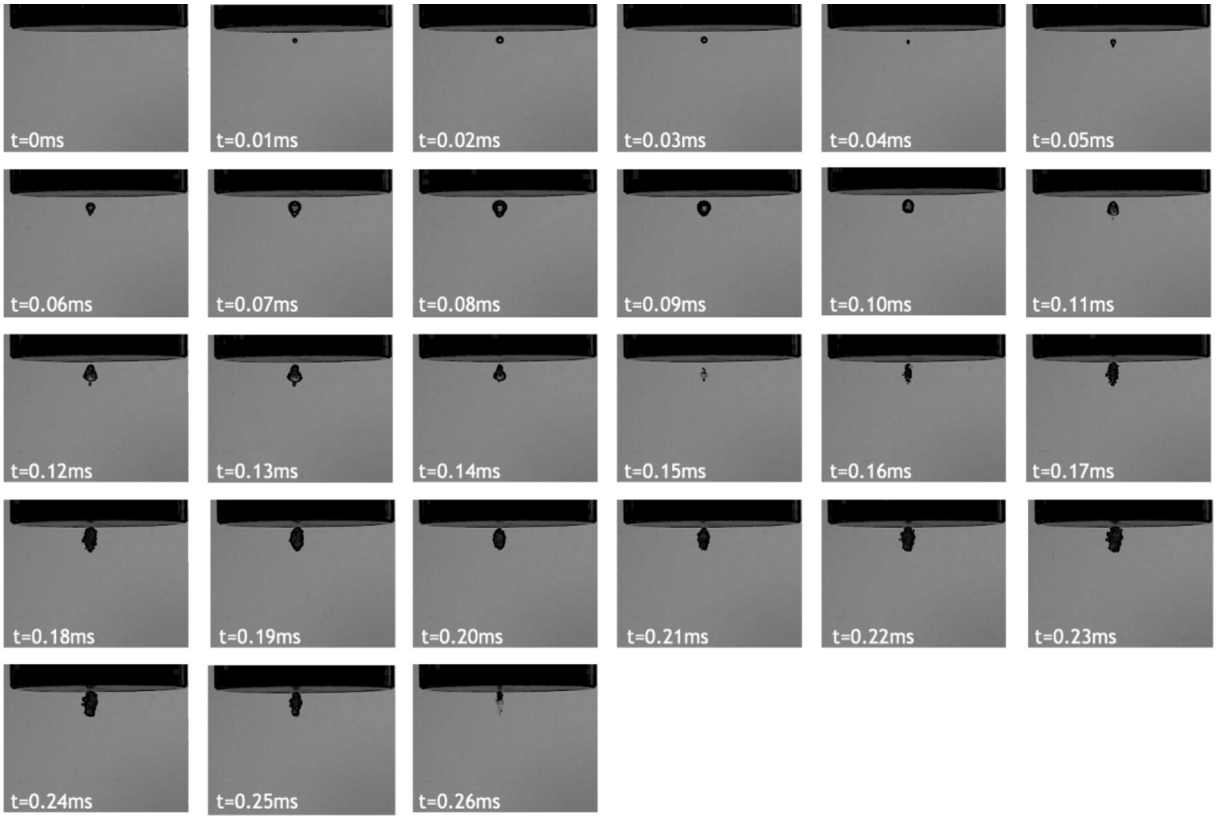

Fig. 5. Cavitation inception in sample with low gas content (condition 1, DO: 4.2 mg/L).

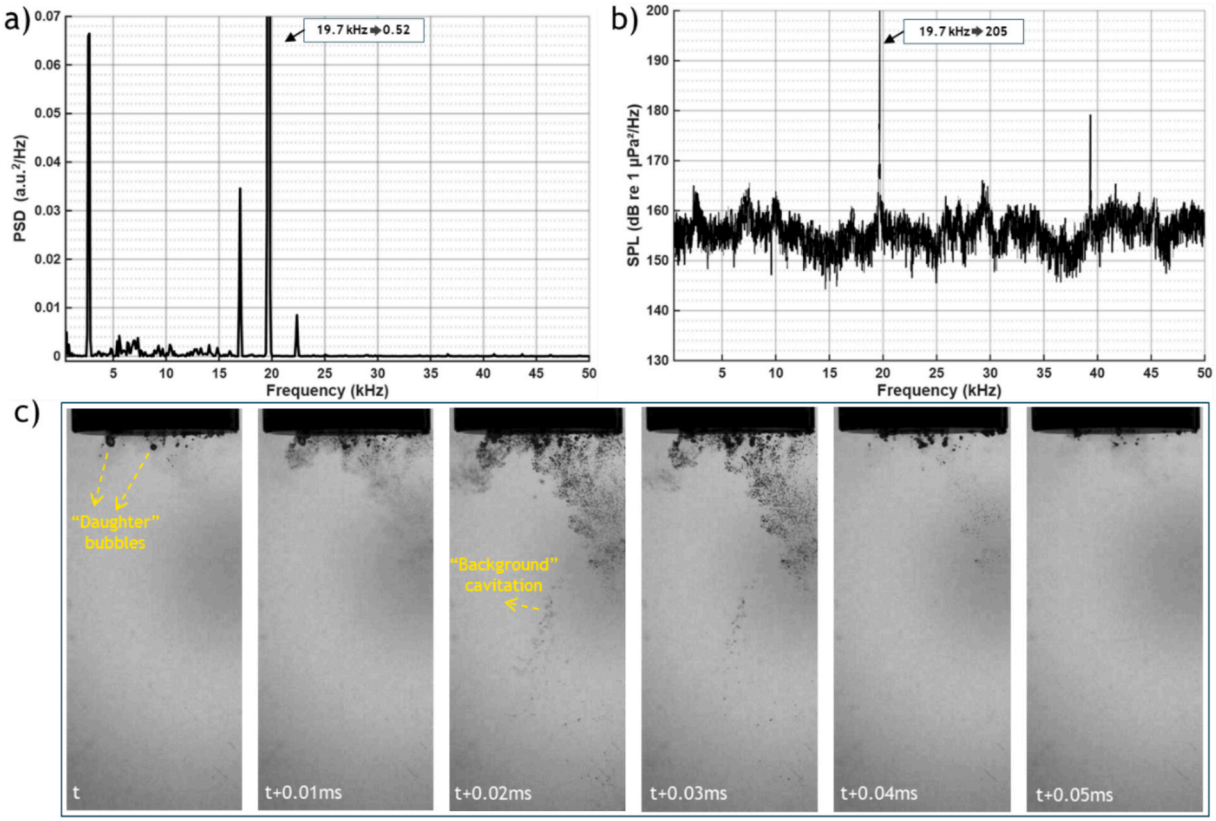

Fig. 6. (a) Power spectrum of grayscale intensity, (b) SPL of acoustic noise, and (c) visualization of one acoustic cycle of cavitation under condition 1.

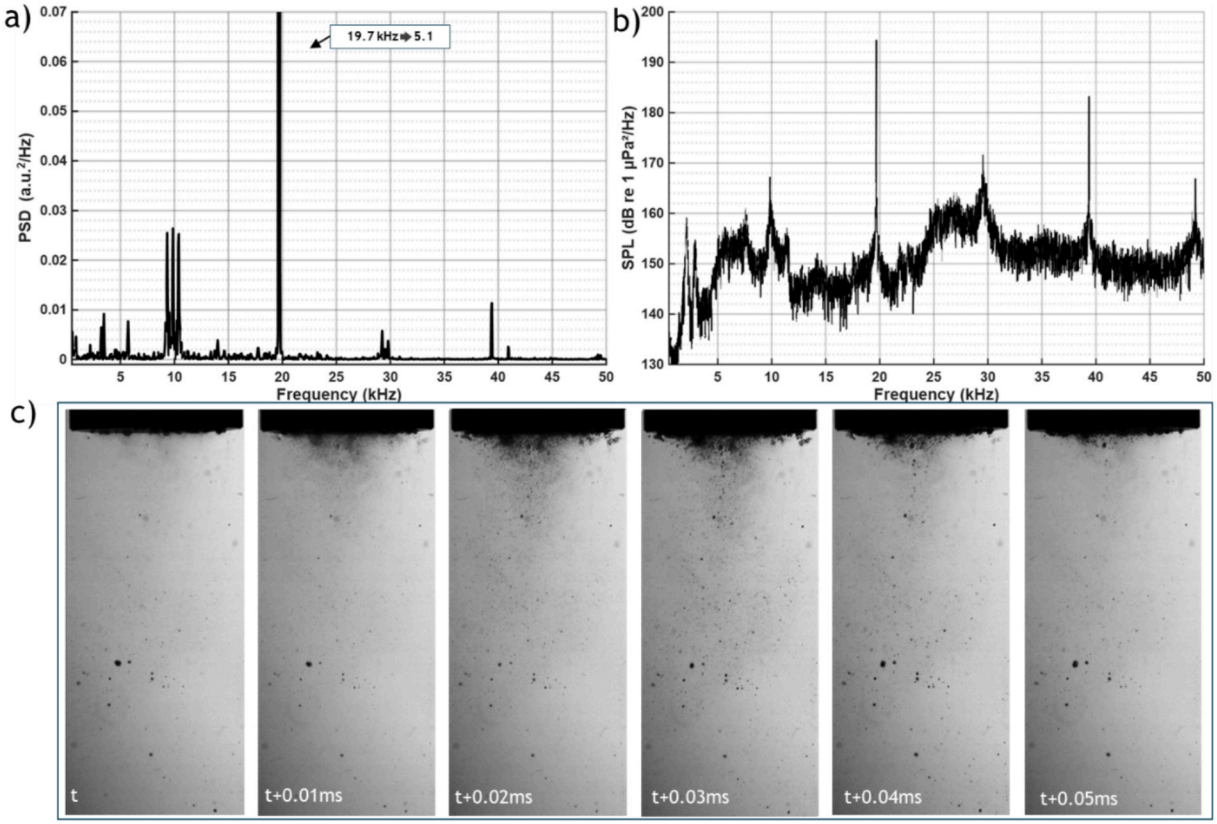

Fig. 7. (a) Power spectrum of grayscale intensity, (b) SPL of acoustic noise, and (c) visualization of one acoustic cycle of cavitation under condition 2.

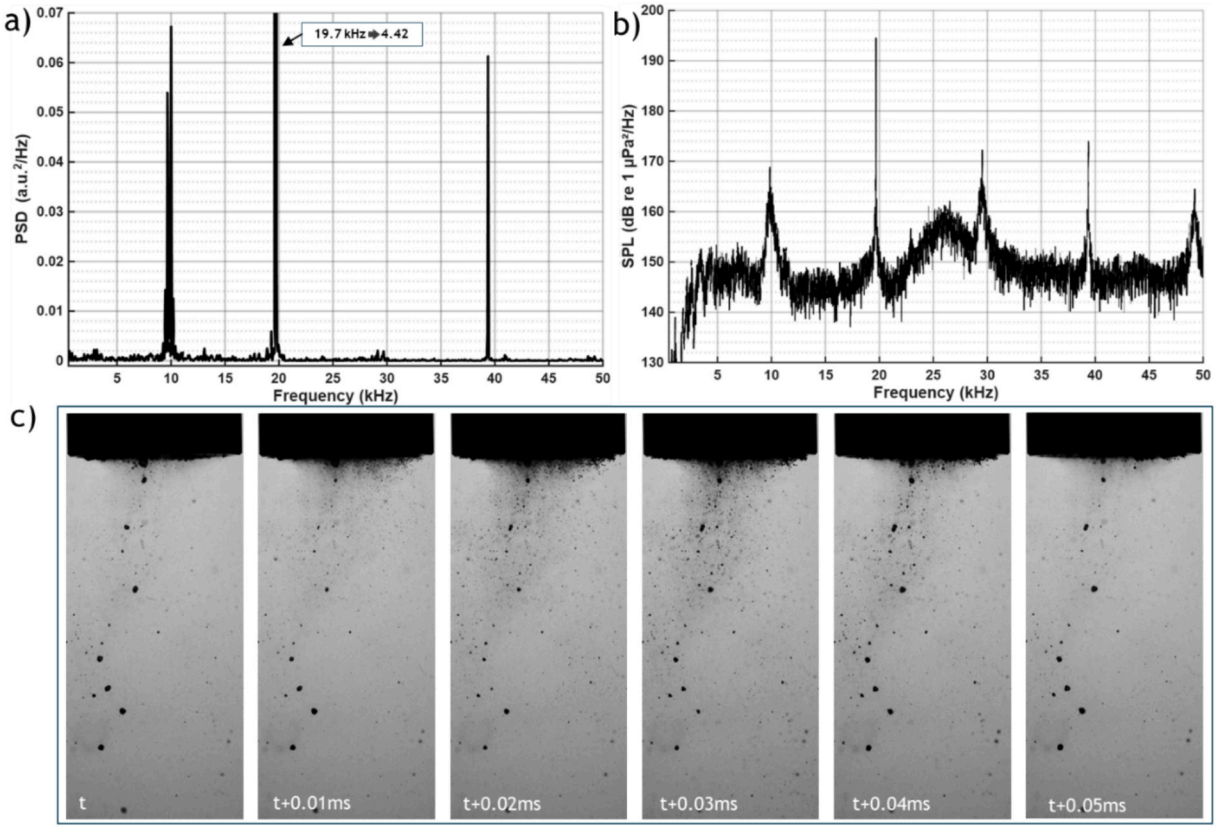

Fig. 8. Power spectrum of grayscale intensity (a), SPL of acoustic noise (b), and visualization of one acoustic cycle of cavitation under condition 3.

subharmonic components are lower in intensity (SPL), and most of the acoustic energy is concentrated at the fundamental (20 kHz) and its second harmonic (40 kHz). This can be attributed to the specific content of the bubble. When the water is degassed, the cavitation bubble's gas–vapor ratio shifts towards vapour. Such bubbles will collapse faster with a less pronounced rebound and reduced bubble oscillation – all due to the lesser amount of condensed gas inside the bubble [22,49].

In the gas saturated condition (Fig. 7, condition 2) the observed cavitation beneath the sonotrode exhibits a more stable behavior – its shape resembles CBS extending downwards.

Compared to condition 1 (Fig. 6), rather than individual bubbles clinging to the sonotrode surface here the attached bubbly layer is formed, promoting the formation of the cloud structure extending downwards. The cavitation cloud oscillates with the driving frequency; however, stable cavitation bubbles also emerge and oscillate over more than one acoustic cycle (compression and rarefaction) – a clear result of high contents of non-condensable gasses inside the bubble, which prevent it to collapse immediately(Can be seen in the Fig. 7c at t = t + 0.5 ms). The noise amplitude at the driving frequency decreases, whereas the corresponding grayscale intensity increases by approximately tenfold compared to condition 1. Moreover, under this condition, the fluctuations in grayscale intensity show an increase at around 10 kHz, corresponding to the $f_0/2$ subharmonic (Fig. 7a). The corresponding acoustic spectrum shows a similar trend, where the subharmonic component around 10 kHz is elevated relative to the baseline (Fig. 7b). Again, this is a result of high ratio of gases against vapor inside the bubble and is in line with previous studies, which often attribute the increase in the $f_0/2$ subharmonic to gaseous cavitation [50–52].

When free air bubbles are present in the liquid, the cavitation beneath the sonotrode develops into a conical shape, oscillating primarily at the driving frequency (Fig. 8c). Moreover, one can see that the number of stable bubbles increases, and they exist for more than one acoustic cycle. The increase in the number of stable bubbles is obviously the contribution of air bubbles present in the liquid. As shown in Fig. 8a, the grayscale intensity rises at 10 kHz ($f_0/2$) and becomes most pronounced at 40 kHz ($2\,f_0$) which is almost six-fold compared to condition 2. However, at the driving frequency (f_0) the gray scale intensity slightly decreases. The corresponding noise data exhibits similar features up to 50 kHz as observed in condition 2, yet some differences can be noted, which are due to the presence of pre-existing air bubbles in the bulk.

The increase in grayscale intensity at 40 kHz indicates a higher population of bubbles oscillating at that frequency. When the corresponding bubble sizes are estimated from the Minnaert frequency, they roughly correspond to diameter of about 165 µm [53]. The presence of pre-existing bubbles in condition 3 clearly supports this, as the bubble size is below 200 µm. The decrease in sound pressure at that frequency can therefore be explained by the presence of these bubbles as they are elastic and absorb sound energy. In this case, the bubbles which have natural frequency near 2 f_0 absorb and scatter acoustic energy most effectively, what leads to a decay around that frequency. This behavior is consistent with theoretical and experimental studies showing maximum attenuation near the bubble's natural frequency and significantly weaker at other frequencies [1,32,54]. Moreover, this phenomenon has also been utilized in previous studies for acoustic bubble spectrum analysis [54]. Based on the same principle it can be deduced that at the driving frequency (20 kHz) the noise intensity compared to condition 2 is not expected to decrease significantly since the pre-existing air bubbles are sub-resonant at that frequency. For 20 kHz the bubble diameter should be roughly 330 µm according to Minnaert equation [53]. The gray scale intensity analysis also supports this observation as in both conditions gray scale intensity values are nearly identical under both conditions. However, at 10 kHz ($f_0/2$), we see higher gray scale intensity at that frequency in condition 3, the peak in the noise spectrum is slightly elevated and broadened compared to condition 2. The change in grayscale intensity is not as high as at 40 kHz, which may explain why the effect is less pronounced. Moreover, the

cavitation bubbles in condition 3 do not collapse completely at the driving frequency but rather at 10 kHz, especially observed at the attached bubble layer on the sonotrode tip, possibly contributing to the increased grayscale intensity at that frequency.

For the higher frequencies (beyond 50 kHz), similar interpretations can be made (Fig. 9). In condition 3, the decrease in broadband "cavitation" noise beyond 30 kHz is promoted. It has been studied, but the underlying mechanism is still not fully understood. It has been suggested that broadband noise results from the emission of strong shock waves and microjets during bubble collapse [43,44]. Consequently, it is mostly associated with transient (inertial) cavitation [55,56]. An increase in broadband high-frequency noise is also regarded as an indicator of cavitation intensity by Komarov et al [57]. Previous studies have also shown that the collapse of a cavitation bubble can be "shielded" by the presence of a nearby air bubble, reducing collapse strength as well as increasing bubble collapse time [25–27]. Recently Luo et al. [26] showed that the cavitation bubble and air bubble could merge, resulting in a decrease in emitted energy and the pressure peak of the shock wave by up to 60 % compared to the bubble-absent condition. Ma et al. [27] further analyzed the cavitation behavior near air bubbles and showed that air bubbles can reduce the collapse intensity even without merging with the cavitation bubble. In both scenarios, the presence of air bubbles influences the emitted shock wave during cavitation bubble collapse, highlighting the significance of air bubble population in the liquid [25]. The observed drop in broadband noise intensity (Fig. 9) can therefore be attributed to both the influence of air bubbles on the collapse intensity of cavitation bubbles and the attenuation and damping of the acoustic waves emitted from the sonotrode. For the latter, many of the pre-existing bubbles have natural frequencies that fall within this high frequency range, which can further contribute to the observed behavior, as discussed previously. The sound pressure curve for condition 4 further supports that the observed broadband decrease is caused by the presence of pre-existing bubbles. In this case, the aerated liquid was mixed, and most of the air bubble content was removed. As shown in Fig. 9, under these conditions, the sound pressure level across the whole frequency range nearly overlaps with the initial state – prior to air sparging (condition 2).

To further quantify these spectral observations, the RMS acoustic pressures were calculated for all conditions. The increase in cavitation noise intensity during degassing has been reported in previous studies [34,35]. As expected, the highest value belongs to the vacuumed sample – 69.2 kPa (condition 1). It is known that, up to a certain DO concentration, the noise intensity and cavitation aggressiveness increase. Many times, it was reported that the threshold lies at approximately half of the saturation level [34,35,58] – around 4.2 mg/L in our case. This behavior was also observed in our experiments, and the vacuumed condition (4.2 mg/L) is therefore presented here as a reference point for the maximum increase in RMS due to gas content related effects. In the air saturated case (condition 2) the RMS value drops to 27 kPa. Under similar DO conditions with pre-existing bubble content (condition 3), the RMS value further decreases to 22.6 kPa. When the pre-existing bubbles were removed through mixing (condition 4), the RMS value increased again to 26.9 kPa (a similar level as condition 2) as expected.

Acoustic intensity (I) is commonly expressed as $I = P_{RMS}^2/\rho c$, where ρ is the density of the liquid and c is the speed of sound [31]. If we assume that the speed of the sound in bubbly liquid (condition 4) here is the same as the condition 3, the acoustic intensity can be considered proportional to the square of the RMS pressure, i.e., $I \propto P_{RMS}^2$. Therefore, under the similar DO conditions, we observed that the acoustic intensity in condition 4 is approximately 30 % lower than in the saturated condition (condition 3). It is worth mentioning that sound speed in a bubbly liquid is typically lower than in a pure liquid, which would further increase the relative difference in acoustic intensity. These results suggest that the pre-existing bubbles in the liquid can lead to reduction in the effective acoustic intensity under similar DO concentrations, likely due to the air bubble–cavitation-bubble and air-bubble–acoustic-field interactions discussed earlier. A similar reduction in the measured acoustic response due to acoustic shielding by bubble clouds has also been discussed in previous studies [59].

It is worth noting that dissolved and undissolved gas content may change dynamically and transition between phases as acoustic cavitation application increases, driven by acoustic degassing and cavitation-induced temperature rise in the liquid [60,61]. In the present study, we therefore focus on the early stages of cavitation where cumulative degassing and thermal effects remain limited, thereby enabling a clearer assessment of the influence of pre-existing gas nuclei on cavitation dynamics. This controlled early-stage analysis is also expected to be valuable for our future study of hydrodynamic cavitation, where undissolved gas bubbles are continuously replenished and temperature-driven gas exchange is not expected to play a dominant role.

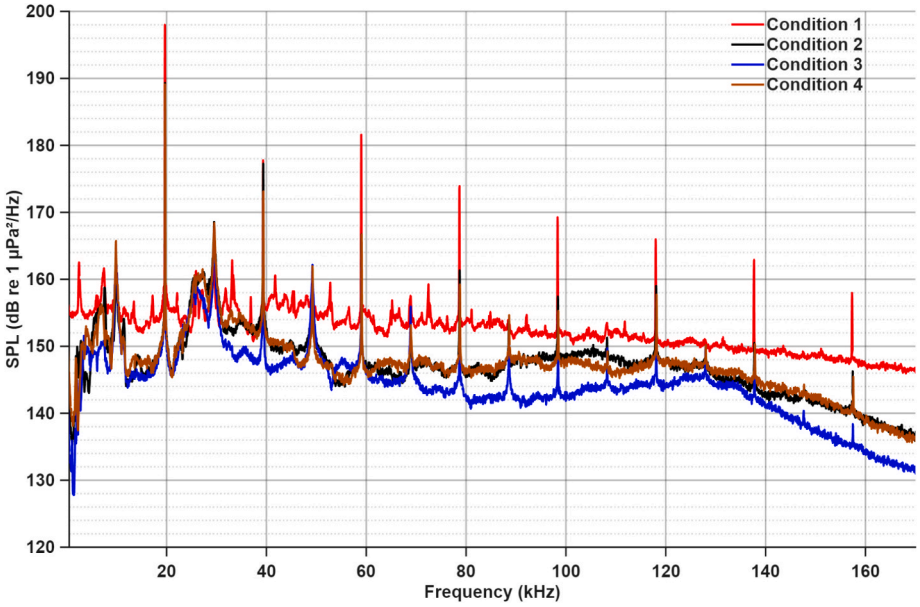

Fig. 9. SPL spectra under four conditions: (1) vacuumed, (2) air-saturated, (3) air-saturated with pre-existing bubbles introduced by air sparging, and (4) air-sparged followed by 10 min mixing after sparging.

To complement this frequency-domain observation, the cavitation beneath the sonotrode was further analyzed for three samples to assess its spatial distribution (using the mean) and temporal variability (using the standard deviation), in order to investigate the effect of pre-existing gas bubbles on cavitation dynamics. The mean value and the standard deviation of gray scale intensity in the images do not change significantly when more than 1500 images are considered. Accordingly, mean intensity and variation maps were created from 2000 consecutive frames of the high-speed image sequences. In the spatial domain, the regions where cavitation activity is strongest obtained by averaging the absolute intensity difference between the consecutive frames are shown in the mean intensity, while the variance maps indicate how much the gray scale intensity in a region deviates from its mean over time. In other words, the mean intensity maps show the spatial location of the strongest cavitation activity, while the variance maps indicate how stable or unstable the cavitation is in those regions.

When the liquid has less dissolved gas and obviously fewer pre-existing free bubbles, as in condition 1, the cavitation observed beneath the sonotrode does not cover the entire sonotrode surface but is rather locally concentrated and appears as individually dispersed bubble structures across the domain. This concentrated region can be seen in Fig. 10a as a dark red area beneath the sonotrode tip. This behaviour can be explained by the absence of nuclei in the bulk liquid; however, daughter bubbles formed after the collapse of previous cavitation bubbles can remain locally in the same region, where they may act as cavitation nuclei and thereby locally intensify the cavitation activity. This localized cavitation activity can also be observed in Fig. 5 after t = 0.15 ms, where cloud cavitation is observed at the location of a collapsing cavitation bubble, following the formation of daughter bubbles.

One can see that cavitation beneath the sonotrode resembles a conical bubble structure (CBS) in the time-averaged image (Fig. 10a). However, the conical appearance results from the mean of multiple consecutive images, whereas the cavitation structure itself is highly dynamic and does not represent stable cavitation formation, as seen in Fig. 6c. Physically this corresponds to mostly vaporous cavitation with intense collapses. Moreover, these dispersed bright isolated regions in Fig. 10b correspond to intermittent local cavitation activities at the frequency discussed previously.

With the increase in the dissolved gas content (condition 2) the

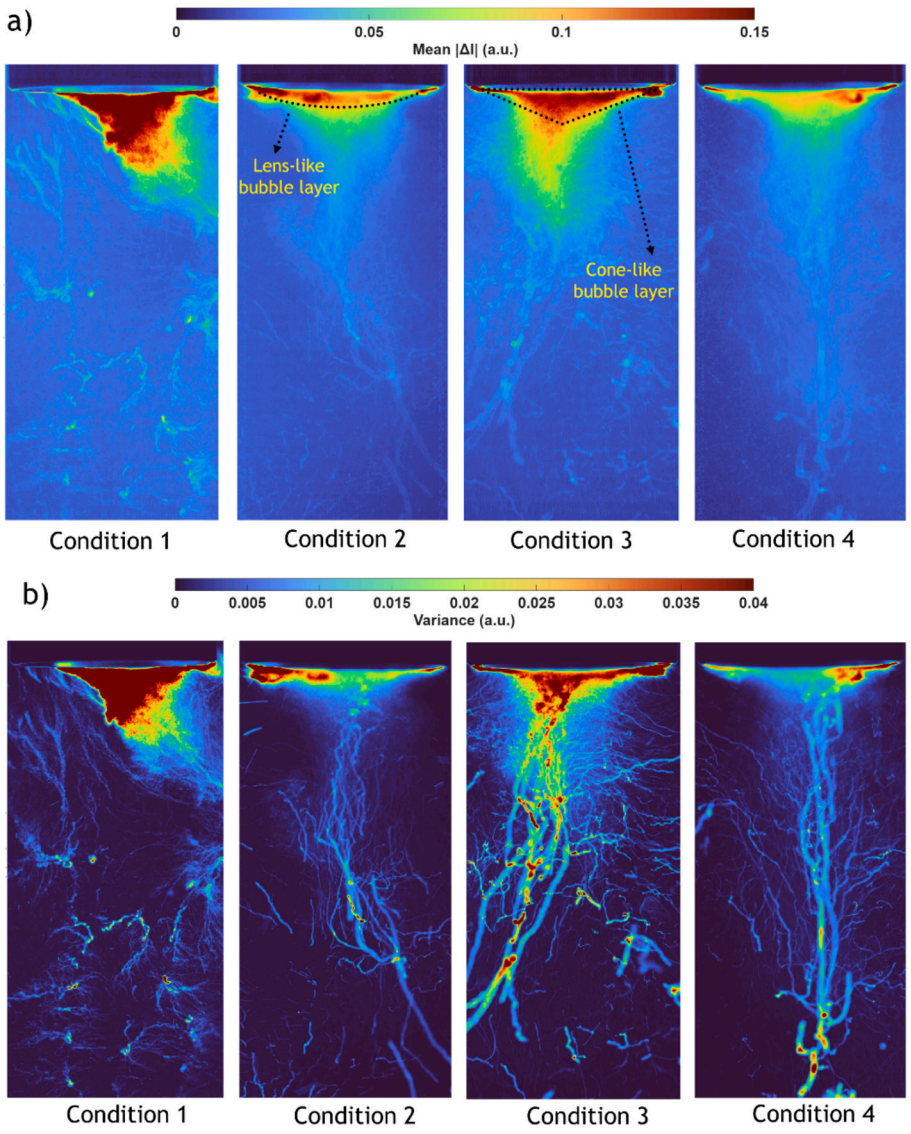

Fig. 10. A) mean intensity maps showing the spatial distribution and location of the strongest cavitation activity and b) Variance maps illustrating the temporal variability of the cavitation activity across the region for conditions 1, 2, 3, and 4.

cavitation resembles CBS where the bubble clusters beneath the sonotrode as mentioned before (Fig. 7c). CBSs are commonly observed in sonotrode cavitation, and their formation and underlying mechanisms have been investigated in previous studies [43,44,62,63]. The structure typically consists of numerous small bubbles that coalesce inside the cone, while a few larger bubbles continue downwards near the central axis, forming a dynamic and self-organizing bubble configuration [64]. Dubus et al. [44] proposed that the nonlinear thickness resonance of the bubble layer on the sonotrode is responsible for the formation of a CBS, and that this layer tends to self-stabilize around its resonance thickness. They showed that the bubble layer has a "lens-like" shape, which focuses the acoustic field close to the sonotrode. According to them, this effect arises from variations in the shape of the bubble layer that introduce inhomogeneities, causing time delays in the acoustic waves and leading to a non-uniform acoustic field distribution. A similar explanation was also reported by Bai et al. [42]. We observed a similar bubble arrangement in the air-saturated condition (condition 2), the agglomeration of the bubbles forms a lens-like shape structure on the sonotrode tip with a lower bubble population at the periphery compared to the center of the sonotrode (Fig. 10a).

When we have the pre-existing air bubbles as in condition 3 the attached cavitation clearly forms CBS (Fig. 10a). However, there are some differences in the CBS dynamics compared to condition 2 discussed previously. As can be seen in Fig. 10a the cavitation has a distinct conical shape exhibiting more extended regions below and horizontally close to the sonotrode tip. One can expect a higher number of nucleation sites in this case due to the presence of air bubbles, which can facilitate cavitation in regions surrounding the central axis. Moreover, in this case, the shape of the bubble layer is no longer lens-like; instead, it resembles a cone-like structure with a higher concentration of bubbles near the center. The cavitation dynamics observed in this region are more vigorous and chaotic (Fig. 10b). We observed that large bubbles tend to accumulate at the center and later detach from the surface. This can also be seen in Fig. 10b, where a higher variance is observed at the center of the sonotrode compared to condition 2, as the bubbles coalesce and grow larger. The growth and coalescence of these bubbles, as previously reported by *Chen* et al. [65], can be attributed to the combined effects of the secondary Bjerknes force and the negative pressure generated during the rarefaction phase of the acoustic cycle [43]. These bubbles are then pushed away from the sonotrode surface. This behavior can be explained by the fact that, as their radius increases beyond the resonance size, the bubbles are no longer attracted toward the cavitation cluster but instead migrate away from the sonotrode tip [65]. This dynamic downward movement of bubbles at the center leads to a deformation of the lens-like shape bubble layer, resulting in the formation of a cone-like shape that extends further downward in condition 3 (Fig. 10a). A similar mechanism was demonstrated previously by Bai et al. [42,43], when artificial nuclei were introduced via a syringe to generate jet-induced bubble clusters, which were then applied to the sonotrode surface. Furthermore, their findings revealed that the cone-like configuration of the bubble layer structure redirects the acoustic field to focus along the axial axis, instead of converging at a single focal point as observed in the lens-like shape bubble layer. Similarly, in our experiments, this region corresponds to the most concentrated and dynamic cavitation activity (Fig. 10b). This behavior was attributed to structural changes in the attached bubble cluster, which modifies the local pressure field and redirects the acoustic radiation forces. They called this structure artificial conical bubble structure (ACBS). Although the mechanism observed here is similar to that of the ACBS, several differences can be noted. This structure was observed only when they implanted nuclei directly beneath the vibrating sonotrode; hence, they referred to it as "artificial." However, in our case, it was observed when pre-existing nuclei were already present in the bulk liquid. According to our observations, these nuclei can have two main effects. As explained previously in Section 3.1, the pre-existing nuclei exhibited a clear tendency to migrate toward the center of the sonotrode where they contribute to bubble coalesce and detachment from the surface. The second effect is the movement of nuclei toward the central axis. We observed that bubbles also move toward the central axis from the surrounding liquid and merge with larger bubbles ejected from the sonotrode. These two types of bubble motion can be seen in Fig. 10b, where bubbles leave trajectories toward the sonotrode tip and dense horizontal trajectories toward the central axis. This bubble–bubble interaction mechanism explains the highly dynamic regions observed in condition 3, as shown in Fig. 10b. Another difference is that Bai et al. [42], reported that ACBS forms artificially in a relatively weak acoustic field which where CBS does not occur spontaneously. The conical structure observed in our experiments develops naturally under stronger acoustic conditions containing pre-existing nuclei. Under the same acoustic parameters, both CBS and this ACBS like structures were observed. In Fig. 10 for condition 2 where we have no pre-existing bubble content and condition 4 where the nuclei content exhibits CBS formation with lens-like shape bubble layer under the same experimental conditions. Moreover, the DO levels are similar in these conditions, suggesting that the presence of pre-existing nuclei alone is responsible for this observation which can alter the cavitation dynamics and change the cavitation structure configuration.

4. Conclusion

The gas content of a liquid can influences cavitation dynamics at all stages, from inception to collapse. In most of previous studies, this effect has been evaluated solely through dissolved gas measurements (usually DO measurements), which cannot capture the contribution of pre-existing undissolved bubbles. In this work, we first examined what can be inferred from DO measurements by using the vacuumed sample (half of the air saturation level, ~ 4.2 mg/L DO) as a reference for the maximum cavitation intensity achievable through dissolved gas control. The primary aim, however, was to investigate the influence of pre-existing gas bubbles on acoustic cavitation dynamics in liquids with identical DO levels, thereby distinguishing their role. For this, small air bubbles below 200 μm diameter were systematically pre-introduced to the water samples. The effect of these bubbles on acoustic cavitation during both the inception and developed phases was investigated using high-speed imaging, with additional hydrophone measurements performed for the developed case.

The results demonstrated that under low DO content and in the absence of undissolved air bubbles, cavitation inception can occur even from a single nucleus. In the developed phase, cavitation predominantly exhibits transient behavior dominated by vaporous cavitation, without forming a stable cavitation bubble structure beneath the sonotrode. This condition also produced the highest overall SPL and RMS acoustic pressure values, indicating the most intense cavitation activity.

The effect of pre-existing gas content was evaluated considering three conditions: before air sparging (air-saturated), after air sparging (with air bubbles), and after mixing the air-sparged liquid to remove the remaining bubble content. Investigation of these conditions revealed that the presence of pre-existing bubbles influences cavitation dynamics by promoting the formation of CBS during the early stages of cavitation. Moreover, in the developed phase these bubbles also influence the cavitation dynamics and structure. Although the observed cavitation structure resembles ACBS, several differences were identified, and the possible contributions of pre-existing bubbles were examined. As main differences, the structure observed in this study was formed naturally and solely from pre-existing bubbles, and this structural variation was observable under the same conditions where the CBS typically appears. Moreover, we also examined their effect on the acoustic noise spectrum and observed that when pre-existing air bubbles are present, the noise spectrum is attenuated and the overall RMS acoustic pressure decreases as well, for which possible explanations are discussed. When the bubble content is removed, the observed differences revert to their initial (air-saturated) state. The results indicate that these effects are reversible and arise from the bubble content, independent of the dissolved gas content,

demonstrating that the DO concentration alone is insufficient to represent the gas-related effects governing cavitation behavior. Therefore, this implies the importance of also characterizing the bubble content prior to cavitation applications.

In future work, we aim to establish robust quantification methods for undissolved bubble populations and extend this framework to hydrodynamic cavitation systems. Moreover, exploring the effects of liquid additives and gas compositions on the mechanical and chemical effects of cavitation could further enhance the understanding of the importance of liquid quality.

CRediT authorship contribution statement

Erçil Toyran: Writing – original draft, Visualization, Investigation, Formal analysis, Data curation, Conceptualization. **Mojca Zupanc:** Writing – original draft, Supervision, Methodology. **Martin Petkovsek:** Writing – original draft, Methodology, Formal analysis. **Matevz Dular:** Writing – original draft, Supervision, Methodology, Funding acquisition, Conceptualization.

Declaration of competing interest

The authors declare that they have no known competing financial interests or personal relationships that could have appeared to influence the work reported in this paper.

Acknowledgements

The authors acknowledge the financial support from the European Union's Horizon Europe research and innovation program under the Marie Skłodowska Curie Grant Agreement No. 101113564 (HORIZON-MSCA-2022-DN-01) and the Slovenian Research and Innovation Agency (Core funding No. P2-0401, P2-0422 and projects No. N2-0381 J2-60032 and N2-0376).

Appendix A. Supplementary data

Supplementary data to this article can be found online at https://doi.org/10.1016/j.ultsonch.2026.107741.

References

[1] F.R. Young, Cavitation (1999), https://doi.org/10.1142/P172.
[2] T.V. Prevenslik, The cavitation induced Becquerel effect and the hot spot theory of sonoluminescence, Ultrasonics 41 (2003) 313–317, https://doi.org/10.1016/S0041-624X(02)00458-4.
[3] N.S.M. Yusof, B. Babgi, Y. Alghamdi, M. Aksu, J. Madhavan, M. Ashokkumar, Physical and chemical effects of acoustic cavitation in selected ultrasonic cleaning applications, Ultrason. Sonochem. 29 (2016) 568–576, https://doi.org/10.1016/J.ULTSONCH.2015.06.013.
[4] G. Mancuso, M. Langone, G. Andreottola, A critical review of the current technologies in wastewater treatment plants by using hydrodynamic cavitation process: principles and applications, J. Environ. Health Sci. Eng. 18 (2020) 311–333, https://doi.org/10.1007/S40201-020-00444-5/TABLES/1.
[5] S. Seyedmirzaei Sarraf, F. Rokhsar Talabazar, I. Namli, M. Maleki, A. Sheibani Aghdam, G. Gharib, D. Grishenkov, M. Ghorbani, A. Koşar, Fundamentals, biomedical applications and future potential of micro-scale cavitation-a review, Lab Chip 22 (2022) 2237–2258, https://doi.org/10.1039/D2LC00169A.
[6] F. Rokhsar Talabazar, C. Baresel, R. Ghorbani, I. Tzanakis, A. Koşar, D. Grishenkov, M. Ghorbani, Removal of per- and polyfluoroalkyl substances (PFAS) from wastewater using the hydrodynamic cavitation on a chip concept, Chem. Eng. J. 495 (2024) 153573, https://doi.org/10.1016/J.CEJ.2024.153573.
[7] R. Terán Hilares, R.M. Dionízio, S. Sánchez Muñoz, C.A. Prado, R. de Sousa Júnior, S.S. da Silva, J.C. Santos, Hydrodynamic cavitation-assisted continuous pre-treatment of sugarcane bagasse for ethanol production: effects of geometric parameters of the cavitation device, Ultrason. Sonochem. 63 (2020) 104931, https://doi.org/10.1016/J.ULTSONCH.2019.104931.
[8] Z. Boček, M. Petkovšek, S.J. Clark, K. Fezzaa, M. Dular, Dynamics of oil–water interface at the beginning of the ultrasonic emulsification process, Ultrason. Sonochem. 101 (2023), https://doi.org/10.1016/j.ultsonch.2023.106657.
[9] Ž. Pandur, I. Dogsa, M. Dular, D. Stopar, Liposome destruction by hydrodynamic cavitation in comparison to chemical, physical and mechanical treatments, Ultrason. Sonochem. 61 (2020), https://doi.org/10.1016/j.ultsonch.2019.104826.
[10] P. Senthil Kumar, M. Siva Kumar, A.B. Pandit, Experimental quantification of chemical effects of hydrodynamic cavitation, Chem. Eng. Sci. 55 (2000) 1633–1639, https://doi.org/10.1016/S0009-2509(99)00435-2.
[11] S.S. Sawant, A.C. Anil, V. Krishnamurthy, C. Gaonkar, J. Kolwalkar, L. Khandeparker, D. Desai, A.V. Mahulkar, V.V. Ranade, A.B. Pandit, Effect of hydrodynamic cavitation on zooplankton: a tool for disinfection, Biochem. Eng. J. 42 (2008) 320–328, https://doi.org/10.1016/J.BEJ.2008.08.001.
[12] J.-P. Franc, J.-M. Michel, Fundamentals of Cavitation 76 (2005), https://doi.org/10.1007/1-4020-2233-6.
[13] M. Dular, M. Petkovšek, Cavitation erosion in liquid nitrogen, Wear 400–401 (2018) 111–118, https://doi.org/10.1016/J.WEAR.2018.01.003.
[14] M. Omelyanyuk, A. Ukolov, I. Pakhlyan, N. Bukharin, M. El Hassan, Experimental and Numerical Study of Cavitation Number Limitations for Hydrodynamic Cavitation Inception Prediction, Fluids 2022, Vol. 7, Page 198 7 (2022) 198. doi: 10.3390/FLUIDS7060198.
[15] A. Šarc, T. Stepišnik-Perdih, M. Petkovšek, M. Dular, The issue of cavitation number value in studies of water treatment by hydrodynamic cavitation, Ultrason. Sonochem. 34 (2017) 51–59, https://doi.org/10.1016/J.ULTSONCH.2016.05.020.
[16] E. Toyran, F.R. Talabazar, I. Tzanakis, M. Ghorbani, A. Koşar, Cavitating flow morphology determination in cavitation-on-a-chip devices based on local real-time pressure measurements, Phys. Fluids 37 (2025), https://doi.org/10.1063/5.0250303/3333648.
[17] A.P. Keller, Cavitation Scale Effects - Empirically Found Relations and the Correlation of Cavitation Number and Hydrodynamic Coefficients, (2001). https://resolver.caltech.edu/CAV2001:lecture.001 (accessed May 29, 2025).
[18] M. Atlar, Final report of the specialist committee on water quality and cavitation. In Pro545 Ceedings of the 23rd ITTC, 2002.
[19] K.R. T., Cavitation, McGraw-Hill, Inc. 6 (1970). https://cir.nii.ac.jp/crid/1572543024529746176 (accessed May 31, 2024).
[20] Y. Zhou, B. Li, Y. Gu, M. Chen, A molecular dynamics simulation study on the cavitation inception of water with dissolved gases, Mol. Phys. 117 (2019) 1894–1902, https://doi.org/10.1080/00268976.2018.1559371;SUBPAGE:STRING:ACCESS.
[21] B. Li, Y. Gu, M. Chen, An experimental study on the cavitation of water with dissolved gases, Exp. Fluids 58 (2017) 1–9, https://doi.org/10.1007/S00348-017-2449-0/FIGURES/10.
[22] T. Trummler, S.J. Schmidt, N.A. Adams, Numerical investigation of non-condensable gas effect on vapor bubble collapse, Phys. Fluids 33 (2021), https://doi.org/10.1063/5.0062399/1064867.
[23] J. Rooze, E.V. Rebrov, J.C. Schouten, J.T.F. Keurentjes, Dissolved gas and ultrasonic cavitation – a review, Ultrason. Sonochem. 20 (2013) 1–11, https://doi.org/10.1016/J.ULTSONCH.2012.04.013.
[24] J.B. Li, W.L. Xu, Y.W. Zhai, J. Luo, H. Wu, J. Deng, Influence of multiple air bubbles on the collapse strength of a cavitation bubble, Exp. Therm Fluid Sci. 123 (2021) 110328, https://doi.org/10.1016/J.EXPTHERMFLUSCI.2020.110328.
[25] J. Luo, W. Lin Xu, R. Li, Collapse of cavitation bubbles near air bubbles, J. Hydrodyn. 32 (2020) 929–941, https://doi.org/10.1007/S42241-019-0061-X/METRICS.
[26] J. Luo, W. Xu, B.C. Khoo, Stratification effect of air bubble on the shock wave from the collapse of cavitation bubble, J. Fluid Mech. 919 (2021) A16, https://doi.org/10.1017/JFM.2021.368.
[27] M. Ma, J. Yin, Y. Zhang, L. Tian, D. Tian, R. Huang, Y. Chen, The shielding effect and interaction mechanism of the air bubble on the cavitation bubble in aeration methods: a numerical study, Phys. Fluids 36 (2024), https://doi.org/10.1063/5.0244941/3325690.
[28] S.L. Ceccio, Friction drag reduction of external flows with bubble and gas injection, Annu. Rev. Fluid Mech. 42 (2010) 183–203, https://doi.org/10.1146/ANNUREV-FLUID-121108-145504/CITE/REFWORKS.
[29] C.Y. Li, S.L. Ceccio, Interaction of single travelling bubbles with the boundary layer and attached cavitation, J. Fluid Mech. 322 (1996) 329–353, https://doi.org/10.1017/S0022112096002819.
[30] M. Arora, C.D. Ohl, D. Lohse, Effect of nuclei concentration on cavitation cluster dynamics, J. Acoust. Soc. Am. 121 (2007) 3432–3436, https://doi.org/10.1121/1.2722045.
[31] L.E. Kinsler, A.R. Frey, A.B. Coppens, J.V. Sanders, Fundamental of Acoustics (2000) 548.
[32] D.T. Laird, P.M. Kendig, Attenuation of sound in water containing air bubbles, J. Acoust. Soc. Am. 24 (1952) 29–32, https://doi.org/10.1121/1.1906842.
[33] E. Hasani Malekshah, W. Wróblewski, M. Majkut, Dissolved air effects on three-phase hydrodynamic cavitation in large scale Venturi- Experimental/numerical analysis, Ultrason. Sonochem. 90 (2022) 106199, https://doi.org/10.1016/J.ULTSONCH.2022.106199.
[34] D. Xia, J. Wu, K. Su, Classification of regimes determining ultrasonic cavitation erosion in aqueous solutions containing dissolved air, Ultrason. Sonochem. 116 (2025) 107324, https://doi.org/10.1016/J.ULTSONCH.2025.107324.
[35] L. Liu, Y. Yang, P. Liu, W. Tan, The influence of air content in water on ultrasonic cavitation field, Ultrason. Sonochem. 21 (2014) 566–571, https://doi.org/10.1016/J.ULTSONCH.2013.10.007.
[36] S.A. Mäkiharju, H. Ganesh, S.L. Ceccio, The dynamics of partial cavity formation, shedding and the influence of dissolved and injected non-condensable gas, J. Fluid Mech. 829 (2017) 420–458, https://doi.org/10.1017/JFM.2017.569.
[37] A. Žnidarčič, R. Mettin, C. Cairós, M. Dular, Attached cavitation at a small diameter ultrasonic horn tip, Phys. Fluids 26 (2014), https://doi.org/10.1063/1.4866270.
[38] M. Li, R. Manica, B. Xiang, Q. Liu, Effect of NaCl and CO2 on the inception control of hydrodynamic cavitation by gas solubility change, Chem. Eng. Sci. 246 (2021) 116997, https://doi.org/10.1016/J.CES.2021.116997.

[39] P.D. Welch, The use of fast fourier transform for the estimation of power spectra: a method based on time averaging over short, modified periodograms, IEEE Trans. Audio Electroacoust. 15 (1967) 70–73, https://doi.org/10.1109/TAU.1967.1161901.
[40] T.G. Leighton, A.J. Walton, M.J.W. Pickworth, Primary bjerknes forces, Eur. J. Phys. 11 (1990) 47, https://doi.org/10.1088/0143-0807/11/1/009.
[41] K. Yasui, Y. Iida, T. Tuziuti, T. Kozuka, A. Towata, Strongly interacting bubbles under an ultrasonic horn, Phys. Rev. E 77 (2008) 016609, https://doi.org/10.1103/PhysRevE.77.016609.
[42] L. Bai, J. Deng, C. Li, D. Xu, W. Xu, Acoustic cavitation structures produced by artificial implants of nuclei, Ultrason. Sonochem. 21 (2014) 121–128, https://doi.org/10.1016/J.ULTSONCH.2013.07.011.
[43] L. Bai, W. Xu, J. Deng, C. Li, D. Xu, Y. Gao, Generation and control of acoustic cavitation structure, Ultrason. Sonochem. 21 (2014) 1696–1706, https://doi.org/10.1016/J.ULTSONCH.2014.02.027.
[44] B. Dubus, C. Vanhille, C. Campos-Pozuelo, C. Granger, On the physical origin of conical bubble structure under an ultrasonic horn, Ultrason. Sonochem. 17 (2010) 810–818, https://doi.org/10.1016/J.ULTSONCH.2010.03.003.
[45] A. Žnidarčič, R. Mettin, M. Dular, Modeling cavitation in a rapidly changing pressure field – Application to a small ultrasonic horn, Ultrason. Sonochem. 22 (2015) 482–492, https://doi.org/10.1016/J.ULTSONCH.2014.05.011.
[46] W. Lauterborn, E. Cramer, Subharmonic route to chaos observed in acoustics, Phys. Rev. Lett. 47 (1981) 1445, https://doi.org/10.1103/PhysRevLett.47.1445.
[47] K. Johnston, C. Tapia-Siles, B. Gerold, M. Postema, S. Cochran, A. Cuschieri, P. Prentice, Periodic shock-emission from acoustically driven cavitation clouds: a source of the subharmonic signal, Ultrasonics 54 (2014) 2151–2158, https://doi.org/10.1016/j.ultras.2014.06.011.
[48] K. Johnston, S. Cochran, P. Prentice, Non-linear cavitation cloud oscillations in high-intensity focused ultrasound, in: IEEE International Ultrasonics Symposium, IUS, 2014, pp. 373–376, 10.1109/ULTSYM.2014.0092.
[49] A. Prosperetti, A. Lezzi, Bubble dynamics in a compressible liquid. Part 1. First-order theory, J Fluid Mech 168 (1986) 457–478, https://doi.org/10.1017/S0022112086000460.
[50] W. Lin, J. Xiao, J. Wen, S. Wang, Identification approach of acoustic cavitation via frequency spectrum of sound pressure wave signals in numerical simulation, Ultrason. Sonochem. 90 (2022) 106182, https://doi.org/10.1016/j.ultsonch.2022.106182.
[51] M. Hodnett, R. Chow, B. Zeqiri, High-frequency acoustic emissions generated by a 20 kHz sonochemical horn processor detected using a novel broadband acoustic sensor: a preliminary study, Ultrason. Sonochem. 11 (2004) 441–454, https://doi.org/10.1016/j.ultsonch.2003.09.002.
[52] J. Frohly, S. Labouret, C. Bruneel, I. Looten-Baquet, R. Torguet, Ultrasonic cavitation monitoring by acoustic noise power measurement, J. Acoust. Soc. Am. 108 (2000) 2012–2020, https://doi.org/10.1121/1.1312360.
[53] M. Minnaert XVI, *On musical air-bubbles and the sounds of running water*, The London, Edinburgh, and Dublin Philosophical Magazine and Journal of Science 16 (1933) 235–248, https://doi.org/10.1080/14786443309462277.
[54] L. D. Rozenberg, ed., Physical Principles of Ultrasonic Technology, 1st ed., Springer US, Boston, MA, 1973. doi:10.1007/978-1-4684-8217-1.
[55] I. Tzanakis, G.S.B. Lebon, D.G. Eskin, K.A. Pericleous, Characterizing the cavitation development and acoustic spectrum in various liquids, Ultrason. Sonochem. 34 (2017) 651–662, https://doi.org/10.1016/j.ultsonch.2016.06.034.
[56] T.G. Leighton, R.E. Apfel, *The acoustic bubble*, J. Acoust. Soc. Am. 96 (1994) 2616, https://doi.org/10.1121/1.410082.
[57] S. Komarov, K. Oda, Y. Ishiwata, N. Dezhkunov, Characterization of acoustic cavitation in water and molten aluminum alloy, Ultrason. Sonochem. 20 (2013) 754–761, https://doi.org/10.1016/J.ULTSONCH.2012.10.006.
[58] K. Yasui, Multibubble sonoluminescence from a theoretical perspective, Molecules 26 (2021) 4624, https://doi.org/10.3390/MOLECULES26154624.
[59] I. Tzanakis, G.S.B. Lebon, D.G. Eskin, K. Pericleous, Investigation of the factors influencing cavitation intensity during the ultrasonic treatment of molten aluminium, Mater. Des. 90 (2016) 979–983, https://doi.org/10.1016/J.MATDES.2015.11.010.
[60] O.V. Abramov, High-intensity ultrasonics: theory and industrial applications, High-Intensity Ultrasonics (2019), https://doi.org/10.1201/9780203751954.
[61] Y. Asakura, K. Yasuda, Frequency and power dependence of ultrasonic degassing, Ultrason. Sonochem. 82 (2022) 105890, https://doi.org/10.1016/J.ULTSONCH.2021.105890.
[62] A. Moussatov, C. Granger, B. Dubus, Cone-like bubble formation in ultrasonic cavitation field, Ultrason. Sonochem. 10 (2003) 191–195, https://doi.org/10.1016/S1350-4177(02)00152-9.
[63] X. Ma, B. Huang, G. Wang, M. Zhang, Experimental investigation of conical bubble structure and acoustic flow structure in ultrasonic field, Ultrason. Sonochem. 34 (2017) 164–172, https://doi.org/10.1016/J.ULTSONCH.2016.05.027.
[64] R. Mettin, Bubble structures in acoustic cavitation, in: Bubble and Particle Dynamics in Acoustic Fields: Modern Trends and Applications, 2005: pp. 1–36.
[65] J. Chen, J. Geng, Y. Li, P. Xia, X. Li, F. Wang, D. Chen, M. Wang, H. Wang, Investigation of incipient cavitation in various liquids based on PIV quantification and numerical simulations, Sci. Rep. 15 (1) (2025) 1–14, https://doi.org/10.1038/s41598-025-93746-3.